*Can. J. Remote Sensing,* Vol. 37, No. 6, pp. 1–16, 2011

# High spatial-and temporal-resolution NDVI produced by the assimilation of MODIS and HJ-1 data

Cai Wenwen, Song Jinling, Wang Jindi, and Xiao Zhiqiang



**Abstract.** The normalized difference vegetation index (NDVI) is widely used in global environmental and climatic change research. However, the 1 km Moderate Resolution Imaging Spectroradiometer (MODIS) is too coarse to quantify changes in heterogeneous landscapes. On the other hand, the 30 m charge-coupled device (CCD) sensor on the Chinese environment satellite (HJ-1) is severely affected by weather, which limits its use in studying the biophysical processes evolving rapidly during the growing season. In cloudy areas, the problem is compounded; only a few images can be obtained for the whole year. It is therefore impossible to obtain the high temporal spatial resolution NDVI required in some applications. To solve this problem, the continuous correction (CC) data assimilation method was proposed to produce high temporal spatial resolution NDVI by combining the advantages of the MODIS temporal information and the CCD spatial information. The MODIS 16 day compositing/8 day windows Nadir BRDF-Adjusted Reflectance and the CCD reflectance were used to predict 8 day/30 m NDVI for the Heihe River basin, China, in 2009. Comparison of predicted data with field data showed that the two were in good agreement. The method demonstrated feasibility, and the NDVI produced provided better vegetation information. The performance of CC depended on the acquisition time and amount of the CCD images.

**Résumé.** L'indice NDVI (normalized difference vegetation index) est utilisé couramment en recherche environnementale et sur les changements climatiques à l'échelle du globe. Cependant, la résolution de 1 km du spectroradiomètre MODIS (Moderate Resolution Imaging Spectroradiometer) est trop grossière pour permettre la quantification des changements dans les paysages hétérogènes. D'autre part, le capteur CCD (dispositif à transfert de charge) à 30 m de résolution monté à bord du satellite environnemental chinois (HJ-1) est sérieusement affecté par la température, ce qui limite son utilisation dans l'étude des processus biophysiques en évolution rapide durant la saison de croissance. Dans les zones nuageuses, le problème est davantage amplifié; seulement quelques images peuvent être obtenues au cours d'une même année. Il est ainsi impossible d'obtenir des mesures de NDVI à la haute résolution temporelle et spatiale nécessaire pour certaines applications. Pour résoudre ce problème, la méthode d'assimilation des données par corrections successives (CC) est proposée pour produire des valeurs de NDVI à haute résolution temporelle et spatiale en combinant les avantages de l'information temporelle de MODIS et l'information spatiale du capteur CCD. Les images composites de MODIS sur 16 jours et les données de réflectance au nadir ajustées pour la FDRB pour des fenêtres de 8 jours ainsi que la réflectance CCD sont utilisées pour prédire les valeurs de NDVI pour 8 jours et à 30 m de résolution pour le bassin du fleuve Heihe, en Chine, en 2009. La comparaison des prédictions avec les données de terrain montre qu'il y a une bonne correspondance entre les deux. La méthode a démontré son utilité et les valeurs de NDVI produites peuvent fournir une meilleure information sur la végétation. La performance de la méthode d'assimilation des données par CC dépend du moment de l'acquisition et de la quantité d'images CCD.
[Traduit par la Rédaction]

## Introduction

The normalized difference vegetation index (NDVI) is routinely produced from red (R) and near-infrared (NIR) data acquired from various kinds of sensors. NDVI time series reveal different temporal and spatial dynamic characteristics according to variations in landscape types (Zhao, 2003), which reveal a certain degree of intra- and inter-annual changes in vegetation (Weiss et al., 2004; Piao et al., 2006). Time series NDVI derived from multiple satellite sensors such as the Advanced Very High Resolution Radiometer (AVHRR), VEGETATION on Satellite Probatoire d'Observation de la Terre (SPOT/VGT), and the Moderate Resolution Imaging Spectroradiometer (MODIS) have proven to be powerful tools in global change-related studies such as vegetation dynamics monitoring (Anyamba and

Received 10 September 2010. Accepted 22 November 2011. Published on the Web at http://pubs.casi.ca/journal/cjrs on 4 April 2012.

**Cai Wenwen, Song Jinling,[1] Wang Jindi, and Xiao Zhiqiang.** State Key Laboratory of Remote Sensing Science, Beijing Key Laboratory for Remote Sensing of Environment and Digital Cities, School of Geography and Remote Sensing Science, Beijing Normal University, Beijing, China.

[1]Corresponding author (e-mail: songjl@bnu.edu.cn).

Vol. 37, No. 6, December/décembre 2011



Tucker, 2005; Martínez and Gilbert, 2009; Lopes et al., 2009), climate change (Potter and Brooks, 1998), land cover mapping and change detection (Defries and Townshend, 1994; Lunetta et al., 2006), and various other fields. However, the coarse resolution of these sensors limits their use in studies of biophysical processes on heterogeneous land surfaces (Shabanov et al., 2003; Doktor et al., 2009). For example, vegetation monitoring is reduced in fragmented landscapes, where most of the pixels are composed of a mixture of different surfaces (Busetto and Meroni, 2008) such as agricultural fields, grassland, or patches of other vegetation as well as unvegetated areas, which are often smaller than moderate-resolution pixels. The 1 km AVHRR from 1990 to 1996 and 200 m land use data are used to investigate the temporal and spatial vegetation dynamics of subclasses using statistical methods (Senay and Elliot, 2000); however, only general trends in vegetation changes over a year can be evaluated using this method. Moreover, the vegetation fraction cannot be accurately estimated from NDVI data because of the nonlinear relationship of NVDI with the vegetation fraction (Jiang et al., 2006) and the saturation effect of NDVI at high biomass (Carlson and Ripley, 1997).

High spatial resolution data such as those from the High Resolution Visible (SPOT/HRV) sensor, the Landsat Thematic Mapper/Enhanced Thematic Mapper (TM/ETM+), and the China–Brazil Earth Resources Satellite (CBERS) can be used for land use and land cover mapping (Oetter et al., 2001; Knorn et al., 2009), ecosystem dynamics monitoring (Stefanov et al., 2005), water quality monitoring (Zhang et al., 2010), and yield estimation (Jarlan et al., 2008; Lopes et al., 2009). The spectral response function of the charge-coupled device (CCD) sensor on the Chinese environment and disaster monitoring and forecasting satellite (HJ-1) is like that of Landsat, SPOT/HRV, and CBERS. This meets the spectral information needs of the vast majority of operational remote sensing applications (Li et al., 2008), including large water body environmental monitoring, aerosol optical thickness inversion studies, and biogeochemical parameter estimation (J. Wang et al., 2010; Q. Wang et al., 2010). HJ-1 data quality was also extensively analyzed and evaluated (Li et al., 2009). The 2–4 day revisit cycle and the 30 m spatial resolution could have made these data much more useful for quantitative remote sensing, but only a few images can be obtained every year in most regions of China because of the vagaries of weather conditions and other constraints. For example, the sensor response is very weak or even nonexistent when surface radiation is low, or the acquired image sometimes has irregular stripes, which is still an unsolved problem. Therefore, the CCD is confronted with the same problem as TM/ETM+, SPOT/HRV, and CBERS, that their temporal resolution (the revisit cycle of Landsat/TM, SPOT/HRV and CBERS is 16 days, 26 days, and 26 days, respectively) is not sufficient for detecting rapid surface changes, especially in frequently clouded areas (Asner, 2001). This limits the usefulness of these devices in studying the rapidly evolving biophysical processes that occur during the growing season.

Most studies that are focused on the generation of high spatial resolution time series data combine high spatial resolution images with frequent revisit coarse-resolution data. A procedure based on classification and regression analysis techniques can be used to generate an NDVI dataset with the spatial resolution of TM images and the temporal resolution of AVHRR data (Maselli and Gilbert, 1998). A semiphysical fusion approach was used to combine the MODIS bidirectional reflectance distribution function (BRDF)/Albedo product with ETM+ data to predict ETM+ reflectance (Roy et al., 2008). The temporal adaptive reflectance fusion model (STARFM, Gao at al., 2006) blends the high temporal resolution of MOD09GHK and the high spatial resolution of TM to predict daily 30 m reflectance data, obtaining good results.

In our study, a data assimilation method with continuous correction (CC, Liang, 2009) was used to combine the temporal information from MODIS and the spatial information from the HJ-1 CCD to produce a high temporal and spatial resolution NDVI to provide more sufficient information for applications that require NDVI both in time and in space, such as timely vegetation fraction estimation. The MODIS 16 day composing/8 day windows 1 km Nadir BRDF-Adjusted Reflectance Product (NBAR) and the HJ-1 CCD 30 m multispectral reflectance data are used mainly to produce an 8 day, 30 m view-geometry removed NDVI dataset. The results have been validated using field measurements and have also been compared with the NDVI generated by STARFM using the same MODIS and HJ-1 CCD data. In the first national soil and water conservation status investigation in China, the 8 day, 30 m vegetation fraction was obtained for a year based on the NDVI dataset produced by CC method. The time resolution of the data generated by STARFM depends on the time resolution of the input MODIS data. However, MODIS daily resolution reflectance data are not suitable for generating NDVI values without correction for the differences caused by observational geometry. This is also why the NBAR was used here instead of the MODIS VI product.

## Study site

A small part of the Heihe River basin (Heihe), Gansu Province, China, located at 38°38′N–39°25′N and 99°50′W–100°50′W, was selected as the study area and is shown in **Figure 1c**. This area is part of the Chinese Simultaneous Remote Sensing and Ground Based Experiment (Heihe experiment) plot shown in the red boxes in **Figure 1b**. Some in situ canopy spectral reflectance data have been measured and can be used to validate the results, as detailed in the Methods section. The study area was approximately 85 km × 85 km, with elevations ranging from 1600 m to 2300 m above sea level. It consists of a

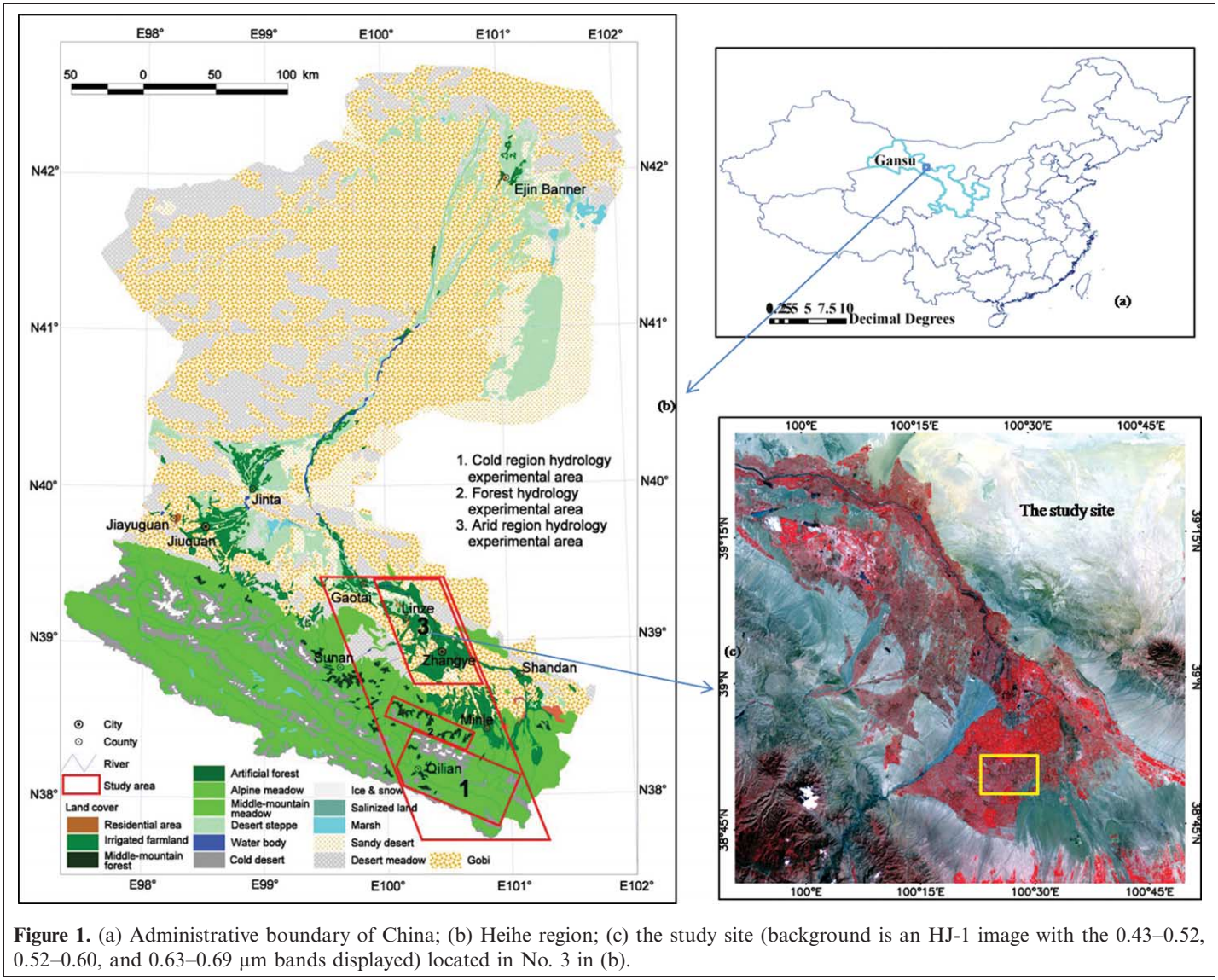


**Figure 1.** (a) Administrative boundary of China; (b) Heihe region; (c) the study site (background is an HJ-1 image with the 0.43–0.52, 0.52–0.60, and 0.63–0.69 μm bands displayed) located in No. 3 in (b).

manmade oasis zone, an oasis–desert transition zone, a desert–grassland zone, and a bare or very sparsely vegetated zone. The land cover types are mainly irrigated land, grassland, forest, and bare or very sparsely vegetated land, as shown in **Figure 2a**. The manmade oasis is a farmland ecosystem, where the crops grown are mainly corn and winter wheat. The dominant vegetation species on the sunny slopes and the shady slopes of the hilly area in the southwestern portion of the region are *Picea crassifolia* and grass, respectively. The local annual average temperature in 2009 was about 6.39 °C and the total precipitation was approximately 187 mm. The meteorological monthly data is shown in **Figure 3**.

## Methods

### HJ-1 NDVI: observations

HJ-1 was launched on 6 September 2008. The HJ-1 mission involves three satellites named HJ-1A, HJ-1B, and HJ-1C; the last is to be launched in the future. The CCD sensors on HJ-1A and HJ-1B provide images with four bands in the visible to near-infrared spectrum and with a ground-swath width of 700 km at a 30 m pixel size.

HJ-1 CCD Level 2 multispectral images were collected in 2009. The Level 2 product was a systematic geometry-correction product and is the highest level product provided to date by the China Center for Satellite Resource Data and Applications. Land-surface reflectance is obtained from a series of processing steps based on the product. First, geometric correction is performed using the ERDAS IMAGINE software. A polynomial correction algorithm is used to correct the data based on ground control points (GCPs) chosen from a 1:100 000 topographic map, while also using a digital elevation model for topographic correction. The correction error is less than one pixel. The results are georeferenced to the universal transverse Mercator (UTM) projection. In the second step, the radiance data is obtained using a linear equation consisting of two calibration coefficients: gain and offset. The coefficients are determined by

Vol. 37, No. 6, December/décembre 2011



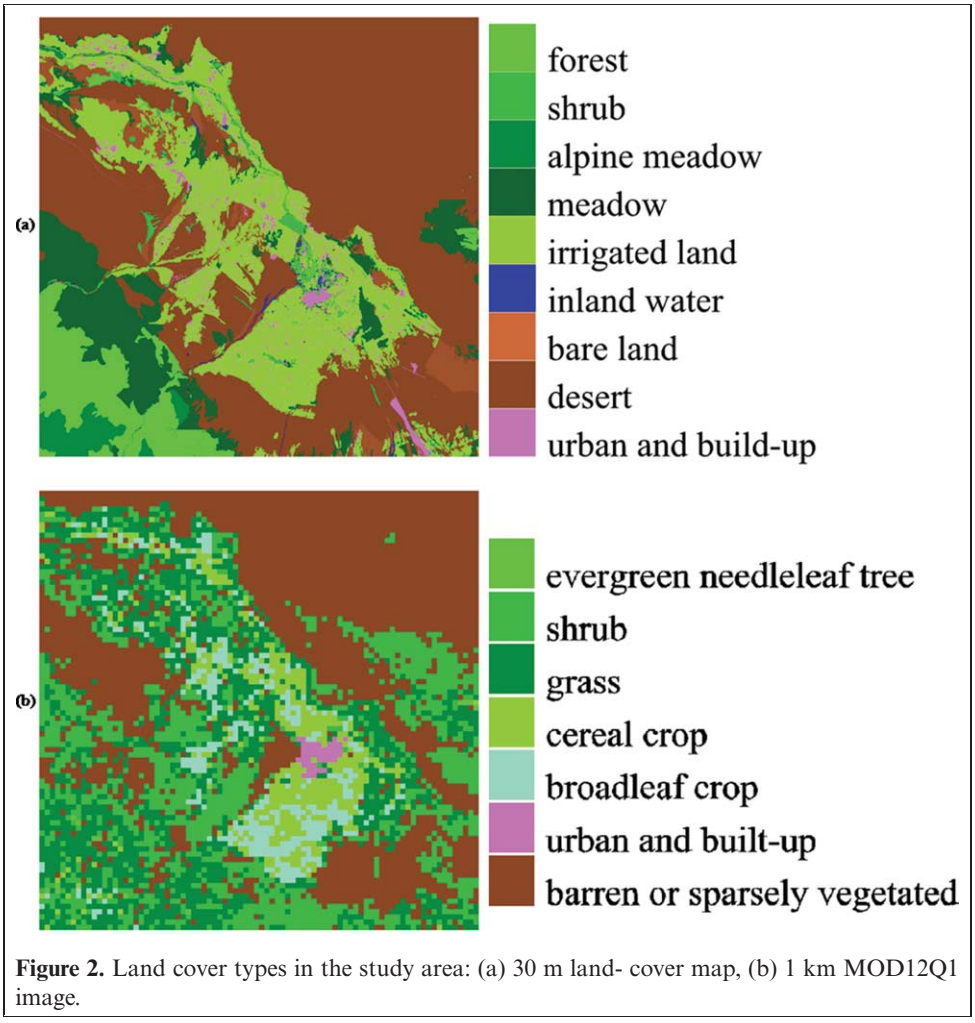


**Figure 2.** Land cover types in the study area: (a) 30 m land- cover map, (b) 1 km MOD12Q1 image.

calibrations carried out in the laboratory and in the field. Finally, surface reflectance is determined as the inverse of the radiance. Atmospheric correction consists of three steps:

1. The top-of-atmosphere (TOA) irradiance at the time of acquisition of the MODIS Terra imagery is obtained using the MODIS onboard calibration

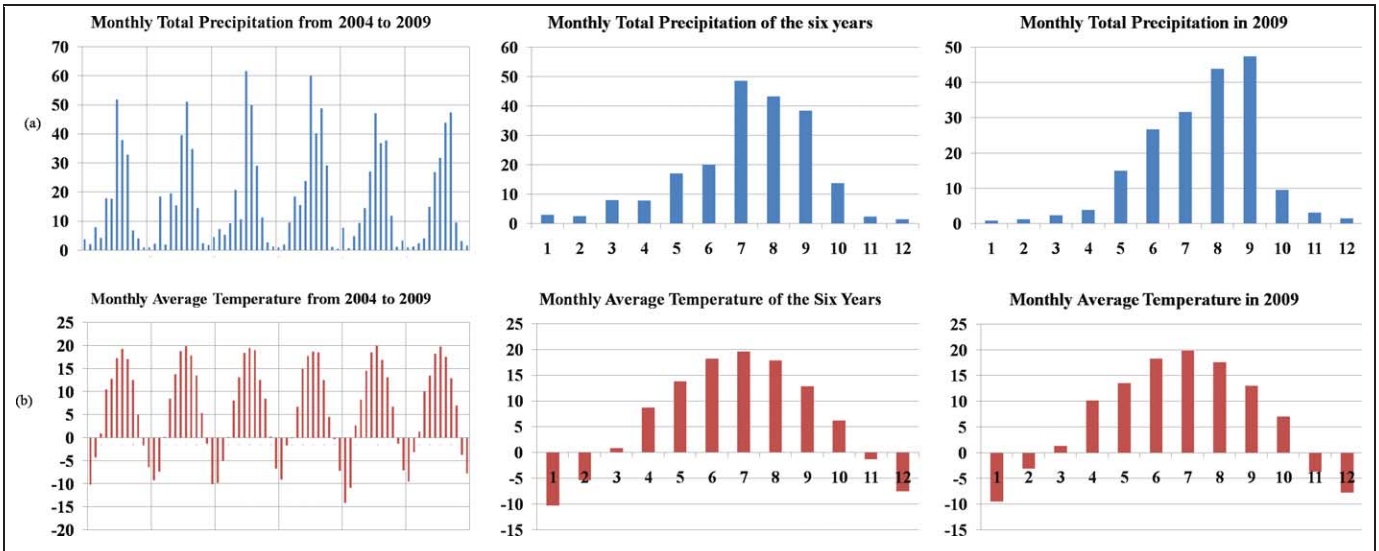


**Figure 3.** Meteorological monthly data of the study area: (a) monthly total precipitation, (b) monthly average temperature.

product. Then, the calibrated MODIS L1B radiance (MOD02) is changed to TOA reflectance.

2. Atmospheric parameters are obtained by inverting the atmospheric radiance transfer model (Lee and Kaufman, 1986) using the MODIS TOA reflectance and MODIS surface reflectance (MOD09). If water or dense vegetation is found in the CCD image, the dark-object method (Liang and Fang, 2001) is used to derive the parameters optically.
3. Because the crossing times of Terra and HJ-1 are both approximately 1030 local time, it is assumed that atmospheric conditions do not change between the two readings. Therefore, the surface reflectance could be derived from the radiance using the atmospheric radiance transfer model with appropriate parameters.

If a sensor looks at the same pixel at the nadir or at a wide angle, the NDVI observed will be quite different. If the NDVI differences are large because of the large field of view (FOV, 30°) of the HJ-1 CCD, these differences must be eliminated to obtain comparable NDVI values. A simple cosine-correction method could be used to perform an angle-effect correction to obtain the nadir-observed NDVI, but the correction is ignored because the selected images covering the study area are part of a scene that is observed almost at the nadir.

The NDVI is an index of the absorptive and reflective characteristics of green vegetation in the R and NIR portions of the electromagnetic spectrum and can be calculated from reflectance measurements as follows:

$$\mathrm{NDVI} = \frac{\rho_{\mathrm{NIR}} - \rho_{\mathrm{R}}}{\rho_{\mathrm{NIR}} + \rho_{\mathrm{R}}} \quad (1)$$

where $\rho_{\mathrm{R}}$ and $\rho_{\mathrm{NIR}}$ are the reflectance of the R and NIR spectral regions, respectively. The HJ-1 CCD NDVI (HJ-1 NDVI) used in CC are produced from reflectance images using Equation (1).

The 30 m land cover map shown in **Figure 2a** was produced by altering a historical land cover map of the study area according to a newly obtained HJ-1 CCD image through visual interpretation. Its overall classification accuracy is 76% as validated by field investigation data. Two hundred control points were determined by a differential global positioning system instrument. The land cover type of each control point was confirmed through field investigation. Estimating the accuracy of the land cover map involves determining whether the categories determined by classification are the same as those confirmed by field investigation for the same locations. The accuracy was not very high because of GPS positioning errors, field investigation errors, and visual interpretation uncertainty.

## MODIS NDVI: background field values

MODIS is a key onboard instrument on the Terra and Aqua satellites designed for global change studies and it monitors land surfaces, the biosphere, the atmosphere, and the seas and oceans once or twice a day. The Level 1A, Level 1B, geolocation, and cloud-mask products along with higher level land and atmospheric products are generated by the MODIS Adaptive Processing System and are parceled out to three Distributed Active Archive Centers (DAAC) for distribution.

All products we used were downloaded from the Land Processes DAAC, including the MODIS 16 day L3 Global 1 km SIN Grid Nadir BRDF-Adjusted Reflectance (NBAR, MCD43B4) and the corresponding quality description product (MCD43B2), from 2004 to 2009, and the MODIS Yearly L3 Global 1 km Land Cover Type product (MOD12Q1) in 2004.

The MOD12Q1 was generated from Terra and Aqua images and incorporates five different land cover classification systems (IGBP, UMD, LAI/FPAR, NPP, and PFT), derived through a supervised decision-tree classification method. The plant functional type (PFT) land cover types included 13 classes defined by the PFT classification system, which included nine vegetation classes, three unvegetated classes, and one unclassified class. The PFT land cover types of the current study area are shown in **Figure 2b**.

The global 1 km gridded and tiled NBAR product is produced every eight days by the MODIS BRDF/Albedo algorithm, which makes use of a semiempirical kernel-driven bidirectional reflectance model and every 16 day acquisitions of multispectral Terra and Aqua images. The high-frequency revisit cycle of MODIS enables acquisition of observations from sufficient looks to form a BRDF for correction of surface reflectance to nadir view. NBAR is more stable and consistent because the directional information has been removed. And NBAR also contains much temporal information about vegetation (Schaaf et al., 2002). NBAR was computed for seven of the MODIS spectral bands (1–7) at the mean solar zenith angle; band 1 (R) and band 2 (NIR) were used.

The quality information in the spectral NBAR was provided by the MCD43B2 dataset and includes band-averaged quality information and band-specific quality information. The band-specific data were coded with 32-bit integer values. Bits 00–03 were used to store band 1 quality, bits 04–07 to store band 2 quality, and so on. The term "quality assessment" (QA) refers to the corresponding values of "bits". In other words, the QA value for each pixel can be 0, 1, 2, 3, or 4. A small QA value indicates better data quality. For any pixel, if its QA flags for the R and NIR bands are both zero, its corresponding NDVI is of the highest quality. Otherwise, the NDVI is of poor quality. Only the highest quality NDVI values are used, thus minimizing the errors caused by poor weather conditions.

The General Cartographic Transformation Package was used to transform the sinusoidal (SIN) projection of all the MODIS products to the UTM projection. Then all the data, including the first two bands of NBAR, the PFT land cover

Vol. 37, No. 6, December/décembre 2011



dataset, and the QA data, were clipped to the extent of the HJ-1 CCD images covering the study area.

Image registration is necessary if different data sources exhibit location errors. There are characteristic lines in MODIS and HJ-1 CCD reflectance images that are helpful in finding the GCPs, thus reducing the registration difficulties due to the enormous difference between MODIS and HJ-1 CCD spatial resolution. The characteristic lines in the two images are displaced only horizontally after the MODIS projection transformation. The Rotate, Scale, and Transform model in the ENVI software was used to correct the MODIS reflectance images according to the GCPs selected from the base-image HJ-1 CCD reflectance data. The same GCPs were applied to the MOD12Q1 and to the QA data. The difference in the MODIS data before and after registration was somewhat hard to distinguish by visualization because the location difference between HJ-1 CCD and MODIS was only one to two MODIS pixels in the horizontal direction. The difference can be ignored. However, if the location difference is substantially large, registration is required. Registration of HJ-1 CCD data and the 30 m land cover map is more important if they are generated from different data sources because CC is conducted one 30 m pixel at a time.

The 1 km NDVI was derived from NBAR using Equation (1). For NBAR, it was necessary first to subtract the offset and then to multiply by the scale factor to obtain the true surface reflectance. It is unnecessary to do this when calculating the NDVI because the offset is zero.

### High spatial and temporal resolution NDVI

The time series NDVI closely tracks the annual cycle of growth and decline of vegetation. The temporal and spatial dynamics of NDVI represent vegetation phenology as it varies from one land cover type to another. The NBAR NDVI can provide 16 day compositing/8 day windows and nadir-observed 1 km measurements for the period from 2004 to 2009. The NDVI time-dynamic model was derived from NBAR and other auxiliary data.

The registered MODIS and the 30 m land cover maps were processed by a program written in the C programming language to output the area percentage image for each category. For example, a MODIS pixel covers $N$ 30 m pixels in space. Assume that the land cover type of the MODIS pixel is $T_a$, that the classes of the 30 m pixels are $T_a$, $T_b$, and $T_c$, and that the numbers of pixels in classes $T_a$, $T_b$, and $T_c$ are $N_a$, $N_b$, and $N_c$, where $N_a + N_b + N_c = N$. Therefore, the area ratios of $T_a$, $T_b$, and $T_c$ in the MODIS pixel are $N_a/N$, $N_b/N$, and $N_c/N$. If the $N$ 30 m pixels all belong to $T_a$ according to a generalized definition such as "grass", the MODIS pixel is judged to be a 100% "pure" pixel in class $T_a$. Prior knowledge of the local is also taken into consideration; for example, there are classes called "cereal crop" and "broadleaf crop" in the PFT classification shown in **Figure 2b**, which are both used because the crops planted in Heihe include not only cereals, but also broadleaf crops. A moving window the size of a MODIS pixel was used, the area ratio for each category in the MODIS pixel was calculated, and the area percentage images were generated by moving the window one pixel at a time. Although the MODIS land cover product and the 30 m land cover map were generated independently and were not produced in the same year, it is not necessary to assume that the land cover types have not changed. Even if they have, the method is feasible as long as the same land cover type exists in both the MODIS and 30 m land cover data sets according to the definition and prior knowledge and as long as pure MODIS pixels of the land cover type in question can be found. The accuracy of the MODIS product used was generally good with respect to the 30 m land cover types and the authors' prior knowledge. The MOD12Q1 contains some classification errors, but they were not considered.

If the area ratio of a category in a MODIS pixel is 100%, or at least greater than 95%, then the NDVI time series and the corresponding QA series of the pixel are derived from the NBAR and the QA data set for the period from 2004 to 2009. The NDVI and QA for all the pure pixels in the category are then extracted. For the dataset with 16 day compositing but on 8 day windows, each pixel represents 46 observations per year and 276 observations over 6 years. The NDVI for each year will be based on less than 46 observations if only the highest quality NDVI is used. However, on the same Julian Day of Year (DOY) in each of the 6 years, there are still observations. It is possible to calculate the average NDVI value and standard deviation (SD) of these observations on the same DOY, as expressed in Equation (2). The six yearly NDVI observations on each DOY are processed in the same way, thus forming a new set of 46 observations which is called here a multiyear average NDVI time series

$$\mathrm{NDVI}^{\mathrm{avg}}(T) = \frac{1}{6 * N} \sum_{I=1}^{N} \sum_{Y=2004}^{2009} \mathrm{NDVI}(I, T, Y) \qquad (2)$$

where the range of $T$ is 1,2,...,46, which is a description of the time in a year, actually $\mathrm{DOY} = T \times 8 - 7$; $N$ is the number of pure MODIS pixels of a land cover type; $Y$ is the year of the data, from 2004 to 2009, NDVI($I$,$T$,$Y$) is the $i$th pure pixel NDVI value at time $T$ in year $Y$, and $\mathrm{NDVI}^{\mathrm{avg}}(T)$ is the average NDVI over the 6 years at time $T$.

The average NDVI is marked as belonging to a particular land cover type because only the NDVI values of MODIS pure pixels in the same category are used to construct it. Every land cover type has its own average NDVI time series and its corresponding SD series, which is called its "NDVI time-dynamic model". The term "time-dynamic model" is just a description of the average NDVI time series, not of the common sense model. Some models are shown in **Figure 4** as examples. Each model represents the changes of its corresponding land cover type in time and in space.

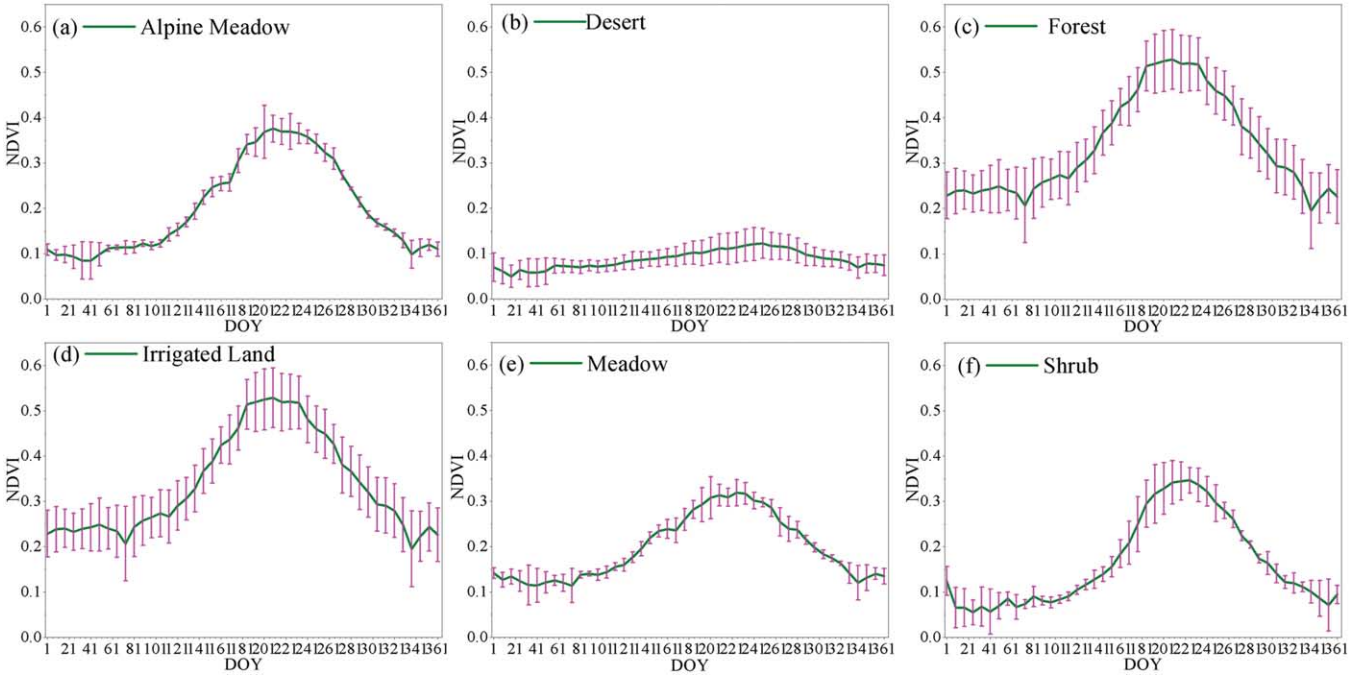


**Figure 4.** NDVI time-dynamic models for six land cover types: (a) alpine meadow, (b) desert, (c) forest, (d) irrigated land, (e) meadow, and (f) shrub.

There are MODIS pure pixels for most of the classes except for shrubs. It is quite reasonable that there are no pure pixels for some land cover types because of the coarse resolution of MODIS and the fragmentation of the land surfaces. Pixel unmixing is therefore needed to obtain subpixel information. Some studies indicate that it is better to use statistical models for large scales (Wan et al., 2008). The linear unmixing model expressed in Equation (3) was chosen to unmix the MODIS mixed pixels to obtain the subpixel NDVI

$$\mathrm{NDVI} = \sum_{i=1}^{n} f_i \mathrm{NDVI}_i + \varepsilon \tag{3}$$

where NDVI represents the NDVI of the mixed MODIS pixel, the end-member $\mathrm{NDVI}_i$ is the NDVI value of the $i$th category in the pixel, $f_i$ is the area ratio of the $i$th category in the pixel, and $\varepsilon$ is an error term.

MODIS shrub pixels were selected from the 1 km land cover map, and the mixed status of these pixels was determined according to the area percentage images. The area ratios of the subpixel classes in these pixels are shown in **Table 1**. Only three pixels are listed, with each line representing the mixed situation of a MODIS shrub pixel. Take the first line in **Table 1** as an example; the end members in the MODIS pixel are shrub, alpine meadow, and desert, and their area ratios are 0.6000, 0.27592, and 0.12408, respectively. The alpine meadow and desert average NDVI time series were extracted and are shown in **Figure 4a** and **4b**. The shrub subpixel NDVI time series were derived by inverting Equation (3) using Equation (4) instead of the commonly used least-squares method. The shrub NDVI time-dynamic model was then calculated as in Equation (4) and is illustrated in **Figure 4f**:

$$\mathrm{NDVI}_{\mathrm{shrub}} = (\mathrm{NDVI}_{\mathrm{MODIS}} - \mathrm{NDVI}_{\mathrm{alpine\ \ meadow}} \times f_{\mathrm{alpine\ \ meadow}} - \mathrm{NDVI}_{\mathrm{desert}} \times f_{\mathrm{desert}}) \Big/ f_{\mathrm{shrub}} \tag{4}$$

To prove that the subpixel NDVI time series is basically the same as the MODIS pure pixel NDVI time series, the MODIS 8 day compositing 250 m surface reflectance (MOD09Q1) from 2004 to 2009 was downloaded from the Land Processes DAAC. The MOD09Q1 includes reflectance for bands 1 and 2 and the corresponding band quality dataset. The data preprocessing method was the same as that used for NBAR and QA. The result was a set of quality-controlled 8 day 250 m NDVI covering the current study area. The pure shrub pixels can be found in the 250 m NDVI. The shrub average NDVI time series was then extracted, and the result is shown as the olive green line in **Figure 5**. The two lines in **Figure 5** are close together, and the correlation coefficient ($R^2$) of the NDVI time series as unmixed from

Table 1. Area ratio of each category in three MODIS shrub pixels*.

| | Category | | | |
|---|---|---|---|---|
| Area Ratio | Shrub | Irrigated land | Alpine meadow | Desert |
| 1 | 0.60000 | 0.00000 | 0.27592 | 0.12408 |
| 2 | 0.48735 | 0.01143 | 0.49224 | 0.00000 |
| 3 | 0.67510 | 0.00000 | 0.00000 | 0.32490 |

*Only three pixels are listed here

Vol. 37, No. 6, December/décembre 2011



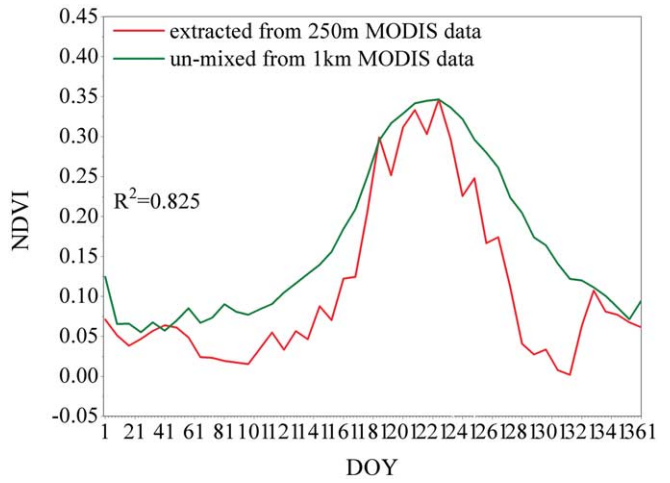


**Figure 5.** Average NDVI time series for shrubs derived from 1 km and 250 m MODIS reflectance images. The olive green line is the multiyear average NDVI time series derived from NBAR, and the pink line is the multiyear average NDVI time series from the 250 m MOD09Q1.

1 km NBAR and the NDVI time series extracted from the 250 m MOD09Q1 is 0.825. The comparison indicated that the inversion method is simple, fast to compute, and effective.

The degree of correlation between MODIS and HJ-1 NDVI is also discussed to confirm to what extent the MODIS NDVI can represent the HJ-1 NDVI. In Heihe, most of the unvegetated region is desert, where the reflectance is stable. The NDVI values at the closest DOY to MODIS and HJ-1 for this category were compared, and the results are shown in **Table 2**. The mean NDVI and SD of all the HJ-1 pixels covered by a MODIS pure desert pixel were calculated. All the pure desert pixels were included. The NDVI $R^2$ of the MODIS pure desert pixels and their corresponding HJ-1 mean NDVI pixels were also calculated on different DOY. The SD value over each MODIS pixel extent was very small, and a very small SD indicates very little change in a 1 km pixel. The $R^2$ values were stable over a period of time, but seem a little low, as shown in the top half of **Table 2**. The reasons why the SD values are small, but the $R^2$ values are only approximately 0.7, may be one or both of the following: (1) the band settings, spectral response functions, and atmospheric correction methods of the two sensors are different, which may cause a difference between MODIS and HJ-1 NDVI; or (2) the calibration coefficients for HJ-1 are still being adjusted, and errors are inevitable. Fortunately, the mean, SD, and NDVI ranges of the two were similar, as shown in the bottom half of **Table 2**. The MODIS R and NIR bands have similar bandwidths to those of the HJ-1 CCD sensor, except that their bandwidths were narrower, as shown in **Table 3**. Therefore, calculating a multiyear average NDVI of the pure pixels is a simple way to obtain the NDVI climatology of a category. Moreover, an NDVI time-dynamic model can represent NDVI changes of a category over time. The model should be adjusted using the HJ-1 CCD spatial information to approximate the real changes of the category in time and in 30 m space.

Data assimilation (DA) can be used to combine the models and the observations. The CC method can consider two data sources simultaneously and can predict highly reliable analytical values over the whole time series. The model can be expressed in the form of Equation (5)

$$X_a(r_i) = X_b(r_i) + \frac{\sum_{j=1}^{n} \varpi\left(r_i, r_j\right)\left[X_o\left(r_j\right) - X_b\left(r_j\right)\right]}{E_o^2/E_b^2 + \sum_{j=1}^{n} \varpi\left(r_i, r_j\right)} \quad (5)$$

where $N$ is the number of observations, the HJ-1 NDVI; $X_o$, $X_b$, and $X_a$ are the observation, background field, and predicted/analysis NDVI, respectively; and $r_i$ and $r_j$ are the prediction date and the observation date, respectively. The weighting factor between MODIS and HJ-1 is $\varpi$, which is set according to the application. $E_o$ and $E_b$ are the errors of the observation and background field data, respectively.

The average NDVI time series of the NDVI time-dynamic model for each category was used as the background field data for the category, and the HJ-1 NDVI of the same category was used as the observations. Errors in the background field data were quantified using the SD series of the NDVI time-dynamic model, and observation errors were assumed to be random Gaussian noise or simply set to a fixed low value. The weighting factor was the inverse of the time distance between background and observation values, specifically described in Equation (6). The predicted NDVI values were generated by entering each category's background field NDVI, observation NDVI, and weighting factor between the two into the model. The category information is provided by the 30 m land cover map.

$$\varpi(r_i, r_j) = \mathrm{abs}\left(r_i - \mathrm{abs}(r_i - r_j)\right)/r_i \quad (6)$$

## NDVI Predicted by STARFM

The STARFM method (Gao et al., 2006) predicts the central pixel value in a window by introducing additional information from homogeneous neighboring pixels, which are weighted according to the spectral difference between TM and MODIS at the same time, the temporal difference between the input time and the time predicted time, and the spatial distance of other pixels to the central pixel in the window, as expressed in Equation (7).

$$H\left(x_{\omega/2}, y_{\omega/2}, t_2\right) = \sum_{i=1}^{\omega}\sum_{j=1}^{\omega}\sum_{k=1}^{n} W_{ijk} \times\left(M\left(x_i, y_j, t_2\right) + H\left(x_i, y_j, t_k\right) - M\left(x_i, y_j, t_k\right)\right) \quad (7)$$

where $\omega$ is the window size, $(x_{\omega/2}, y_{\omega/2})$ is the central pixel of the window; $W_{ijk}$ is the weight, which is a multiplier

**Table 2.** Statistical analysis of MODIS and HJ-1 desert NDVI.

| NDVI correlation on different DOY | | | | | | | | | | |
|---|---|---|---|---|---|---|---|---|---|---|
| MODIS NDVI | 65 | 73 | 121 | 145 | 153 | 161 | 169 | 177 | 204 | 209 |
| HJ-1 NDVI | 66 | 76 | 123 | 142 | 152 | 158 | 168 | 179 | 201 | 208 |
| R2 | 0.687 | 0.643 | 0.661 | 0.623 | 0.674 | 0.692 | 0.699 | 0.664 | 0.600 | 0.625 |

| NDVI statistics on different DOY | | | | | |
|---|---|---|---|---|---|
| Statistic | DOY | Minimim | Mean | Maximum | SD |
| MODIS NDVI | 65 | 0.042 | 0.077 | 0.119 | 0.012 |
| HJ-1 NDVI | 66 | 0.042 | 0.067 | 0.095 | 0.008 |
| Difference | | −0.012 | 0.010 | 0.055 | 0.011 |
| MODIS NDVI | 73 | 0.042 | 0.076 | 0.114 | 0.012 |
| HJ-1 NDVI | 76 | 0.070 | 0.094 | 0.125 | 0.011 |
| Difference | | −0.040 | −0.018 | 0.016 | 0.009 |
| MODIS NDVI | 121 | 0.041 | 0.095 | 0.217 | 0.025 |
| HJ-1 NDVI | 123 | −0.008 | 0.019 | 0.099 | 0.014 |
| Difference | | −0.012 | 0.076 | 0.210 | 0.025 |
| MODIS NDVI | 145 | 0.038 | 0.106 | 0.310 | 0.040 |
| HJ-1 NDVI | 142 | 0.042 | 0.092 | 0.205 | 0.019 |
| Difference | | −0.089 | 0.015 | 0.231 | 0.037 |
| MODIS NDVI | 153 | 0.044 | 0.113 | 0.318 | 0.045 |
| HJ-1 NDVI | 152 | 0.012 | 0.048 | 0.155 | 0.020 |
| Difference | | −0.032 | 0.064 | 0.277 | 0.042 |
| MODIS NDVI | 161 | 0.053 | 0.119 | 0.389 | 0.051 |
| HJ-1 NDVI | 158 | 0.003 | 0.039 | 0.166 | 0.024 |
| Difference | | −0.029 | 0.080 | 0.329 | 0.048 |
| MODIS NDVI | 169 | 0.054 | 0.121 | 0.394 | 0.054 |
| HJ-1 NDVI | 168 | −0.002 | 0.048 | 0.214 | 0.028 |
| Difference | | −0.004 | 0.073 | 0.348 | 0.052 |
| MODIS NDVI | 177 | 0.054 | 0.127 | 0.438 | 0.063 |
| HJ-1 NDVI | 179 | −0.044 | 0.001 | 0.170 | 0.031 |
| Difference | | 0.012 | 0.126 | 0.446 | 0.062 |
| MODIS NDVI | 201 | 0.052 | 0.127 | 0.433 | 0.071 |
| HJ-1 NDVI | 204 | 0.054 | 0.114 | 0.444 | 0.051 |
| Difference | | −0.295 | 0.013 | 0.309 | 0.068 |
| MODIS NDVI | 209 | 0.045 | 0.126 | 0.440 | 0.070 |
| HJ-1 NDVI | 208 | 0.062 | 0.117 | 0.469 | 0.052 |
| Difference | | −0.334 | 0.009 | 0.292 | 0.067 |

factor of the spectral difference between $H(x_i, y_j, t_k)$ and $M(x_i, y_j, t_k)$, the temporal difference between $M(x_i, y_j, t_0)$ and $M(x_i, y_j, t_k)$ $M(x_i, y_j, t_2)$ and the local distance difference between $(x_i, y_i)$ and $(x_{\omega/2}, y_{\omega/2})$ in the window; $M(x_i, y_j, t_k)$ is NBAR NDVI at time $t_2$, $H(x_i, y_j, t_k)$ and $M(x_i, y_j, t_k)$ is the HJ-1 and NBAR NDVI at the high spatial resolution data acquisition time $t_k$. More detailed information is in Gao et al. (2006).

All poor quality NBAR NDVI pixels were removed according to their QA, that is, only those pixels having QA values for the R and NIR bands both equal to zero were retained. There was no QA layer in the HJ-1 image, and therefore certain errors such as cloud contamination could be introduced. The NBAR NDVI and the HJ-1 NDVI used in the CC were combined by means of the STARFM method, and parts of the results are shown in **Figure 6a**.

## Field NDVI

To validate the accuracy of the predicted NDVI, some in situ canopy spectral reflectance values measured in the Heihe experiment were used (Li et al., 2009). Several sites are located there, but only one of these could provide time-series measurements, which are shown in the yellow box (YK) in **Figure 1**. The other sites were also able to provide

**Table 3.** HJ-1 CCD bandwidth and MODIS bandwidth.

| HJ-1 CCD Band | CCD Bandwidth (nm) | MODIS Band | MODIS Bandwidth (nm) |
|---|---|---|---|
| 1 | 430 – 520 | 3 | 459–479 |
| 2 | 520–600 | 4 | 545–565 |
| 3 | 630–690 | 1 | 620–670 |
| 4 | 760–900 | 2 | 841–876 |

Vol. 37, No. 6, December/décembre 2011



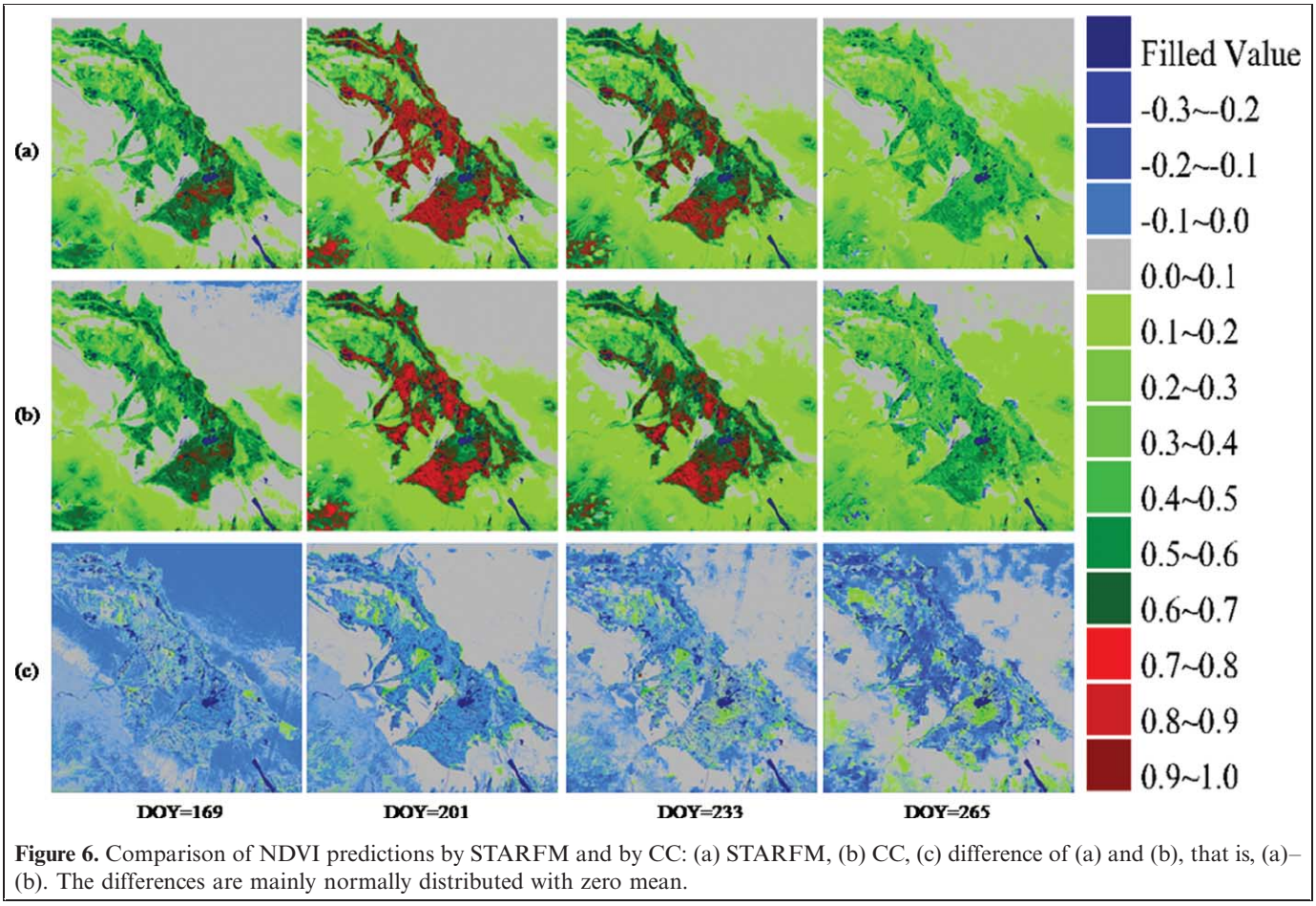


**Figure 6.** Comparison of NDVI predictions by STARFM and by CC: (a) STARFM, (b) CC, (c) difference of (a) and (b), that is, (a)–(b). The differences are mainly normally distributed with zero mean.

some discrete measurements, but they were insufficient to be used for validation.

The spectral reflectance was measured approximately once every 10 days between April and July 2008 using the FieldSpec spectrometer developed by the Analytical Spectral Device (ASD) Inc. The ASD FieldSpec is a hyperspectral field experiment device with a wavelength range of 350–2500 nm. It was set to a 25° FOV, observing nadir direction and was handheld in the experiment. The hyperspectral field reflectance measurements were processed using the HJ-1 CCD spectral response function to convert them to band reflectance values corresponding to the CCD sensor. The reflectance of band $i$ can then be calculated as

$$\rho_i = \sum_{\lambda=\lambda_{S_i}}^{\lambda_{T_i}} r(\lambda)\varphi_i(\lambda) \Big/ \sum_{\lambda=\lambda_{S_i}}^{\lambda_{T_i}} \varphi_i(\lambda) \tag{8}$$

where $\rho_i$ is the calculated reflectance of band $i$, $\lambda_{S_i}$ is the start wavelength of band $i$, $\lambda_{T_i}$ is the end wavelength of band $i$, $r(\lambda)$ is the reflectance at wavelength $\lambda$, and $\varphi_i(\lambda)$ is the HJ-1 CCD spectral response factor at wavelength $\lambda$.

The field NDVI was then calculated from the band reflectance $\rho_i$ using Equation (1). Field measurements were affected by various factors, for example, the measurement target was vegetation canopy or soil, so the measurement results can vary. Multiple measurements were taken in 30 m space, and a simple average was chosen to represent the pixel NDVI. A 16 day maximum value composite filter was applied to the field NDVI to reduce observation errors and to facilitate comparison with the predicted NDVI at the same temporal resolution. The uncertainty arose mainly from the measurement process and the measurement environment.

## Results and discussion

The high-resolution NDVI generated by the CC method is shown in **Figure 7**. As visualized in **Figure 7**, the changes in time and space of the onset of greenness, peak, and senescence of vegetation are identified by the predicted NDVI. For example, consider the main vegetation cover type, irrigated land, where the main crops are winter wheat and corn. March to September is the main growing period of vegetation on the irrigated land. Winter wheat is sown in March and comes to the heading and filling stage in early May to late June and then gradually matures. Finally, its growth phase ends in late July. Corn grows from May to September. It emerges in early May, comes to the heading and filling stage while the wheat is being harvested, and then gradually matures until its harvest season in late August.

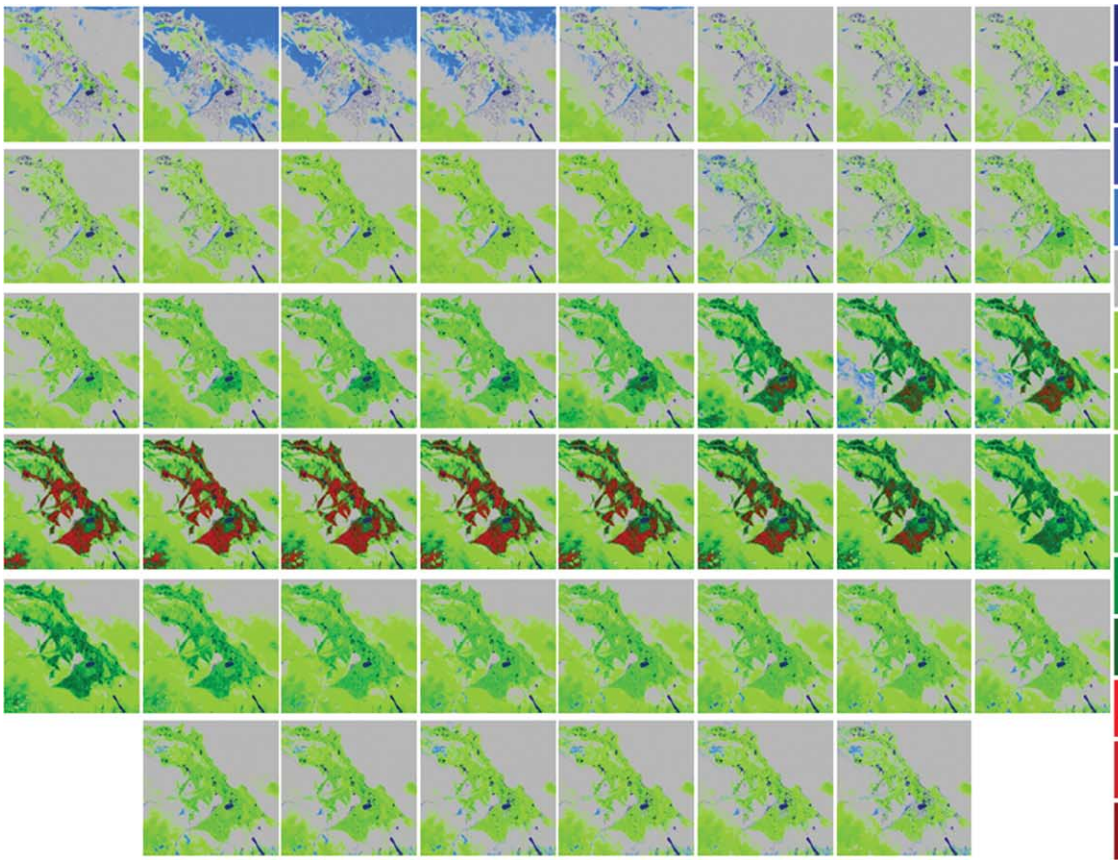


**Figure 7.** Eight day, 30 m NDVI maps, DOY = 1 to DOY = 361 (from top to bottom and left to right), with data recorded every eight days. In the legend, "Filled Value" represents inland water and urban land. These areas are not of interest and are not studied. Low NDVI values in forest and alpine meadow areas may be caused by cloud contamination in the HJ-1 NDVI used for CC.

In other words, higher NDVI values appear from late June to late August in most irrigated land regions, which is clearly evident (corresponding to maps 24 through 31) in **Figure 7**.

The validation of the predicted NDVI consists of two parts. The first part is the comparison of the predicted NDVI with the images acquired by the HJ-1, which is called "image validation". The second part, called "in situ validation", involves comparison of the predicted NDVI with the field NDVI. Image validation indicates the extent to which the predicted NDVI retains the information from the CC-used HJ-1 NDVI and how well the predicted NDVI performs compared with the CC-do-not-use HJ-1 NDVI. In situ validation indicates the accuracy of the predicted NDVI.

### Image validation

Twenty of the 38 HJ-1 images available were affected by cloud and other data quality problems and were discarded. The remaining good quality data consisted of 10 images providing full coverage of the study area and 8 images providing only partial coverage due to the satellite orbit and were used in two ways.

1) The ten images were used in CC to produce a high spatial and temporal resolution NDVI. To facilitate understanding, these ten images are called the "image NDVI", and the high-resolution NDVI is called the "predicted NDVI". The $R^2$ of the predicted NDVI and the image NDVI on the closest DOY were calculated and are listed in **Table 4**. Each column, except for the first two, represents statistics on different dates within a category. The $R^2$ values of all land cover types were almost all greater than 0.9, which indicated that the predicted NDVI had captured the spatial information in the image NDVI. Because only one image NDVI was used to predict the NDVI of the vegetation categories over a short time and because more than one image NDVI was used to predict the bare land and desert NDVI over the whole time period, the $R^2$ values of these two categories were lower than those of the other categories.

The mean and SD of each category were also statistically determined. There were only slight variations among the SD values for each category, and the magnitude was $\pm 0.03$ and even $\pm 0.01$ for some categories. These values indicated that the predicted NDVI can retain the spatial characteristics of the image NDVI because the SD can be considered to reflect

Vol. 37, No. 6, December/décembre 2011



**Table 4.** Correlation coefficients for all land cover types of the predicted NDVI and image NDVI.

| No. | DOY–category* | Meadow | Alpine meadow | Shrub | Forest | Irrigated land | Bare land | Desert |
|---|---|---|---|---|---|---|---|---|
| 1 | 065–066 | 1.000 | 1.000 | 1.000 | 1.000 | 1.0000 | 0.809 | 0.955 |
| 2 | 073–076 | 0.944 | 0.985 | 0.970 | 0.913 | 0.987 | 0.869 | 0.957 |
| 3 | 121–123 | 0.981 | 0.990 | 0.992 | 0.993 | 0.997 | 0.810 | 0.997 |
| 4 | 145–143 | 0.975 | 0.970 | 0.989 | 0.966 | 0.978 | 0.852 | 0.845 |
| 5 | 153–152 | 1.000 | 1.000 | 1.000 | 1.000 | 1.000 | 0.899 | 0.896 |
| 6 | 161–158 | 1.000 | 1.000 | 1.000 | 1.000 | 1.000 | 0.930 | 0.908 |
| 7 | 169–168 | 1.000 | 1.000 | 1.000 | 1.000 | 1.000 | 0.959 | 0.941 |
| 8 | 177–179 | 1.000 | 1.000 | 1.000 | 1.000 | 1.000 | 0.969 | 0.950 |
| 9 | 201–204 | 1.000 | 1.000 | 1.000 | 1.000 | 1.000 | 0.903 | 0.908 |
| 10 | 209–208 | 1.000 | 1.000 | 1.000 | 1.000 | 1.000 | 0.906 | 0.893 |

*The number at the left of "–" is the DOY of the predicted NDVI and the number at the right of "–" is the DOY of the HJ-1 NDVI.

spatial variations. The differences between the mean values of each category were mainly between −0.05 and +0.05.

2) The eight images were not used in CC, but were used in image validation. Similar to the previous step, these eight images are called the "validation NDVI", and the high resolution NDVI is called the "predicted NDVI". The NDVI of the zone of overlap between the predicted and validation NDVIs on the closest DOY were compared. The $R^2$ values were also calculated as in step 1, and the results are shown in **Table 5**.

In Heihe, forest and alpine meadow areas were sometimes affected by cloud cover and cloud shadows. The clouds in the image NDVI were not removed, and therefore they could introduce some noise into the predicted NDVI; this explains why most of the $R^2$ values of the two categories were low. As shown in the first line of **Table 5**, the $R^2$ values of forest (0.857) and alpine meadow (0.874) were much higher than that of the two categories on the other dates because the image NDVI used to generate the predicted NDVI on DOY 129 and the validation NDVI on DOY 125 were both cloud free.

Compared with alpine meadow and forest, the $R^2$ values for meadow, shrub, and irrigated lands were higher over a period of time, which indicated that the predicted NDVI and the validation NDVI were in good agreement. The $R^2$ values varied slightly among the different types, and were different at different times for the same category.

The high $R^2$ indicated that the predicted NDVI could achieve a very close approximation to the HJ-1 measurements. The background field data of these categories were quality controlled, and the 30 m NDVI observations were selected cloud-free, high-quality data. It was concluded that the predicted NDVI of these categories were similar to the cloud-free, 30 m, nadir-observed NDVI. It was necessary to use high-quality NDVI observations in CC. If completely cloud-free images for every category were used, the results would be much better. However, completely cloud-free images are not easy to obtain, so future work by the authors will involve trying to remove the clouds and cloud shadows from the HJ-1 CCD images (Ri et al., 2010).

The mean and SD of every land cover type in the predicted NDVI and the validation NDVI on the closest DOY were statistically determined. The differences are shown in **Figures 8a** and **8b**. It is apparent that SD was conserved with spatial variations. Therefore, it was concluded that the predicted NDVI provided a good approximation to the spatial characteristics of the corresponding time validation NDVI while maintaining accurate numerical values. The difference may be caused by the differences between the image NDVI and the validation NDVI as well as by the introduction of MODIS course information, because the information in the predicted NDVI was obtained from the image NDVI and the MODIS background field NDVI.

### In situ validation

The time series of the four pixels (matching the four plots in YK) in the predicted NDVI are shown in **Figure 9**.

**Table 5.** Correlation coefficients for all land cover types of the predicted NDVI and validation NDVI.

| No. | DOY–category* | Meadow | Alpine meadow | Shrub | Forest | Irrigated land | Bare land | Desert |
|---|---|---|---|---|---|---|---|---|
| 1 | 129–125‡ | 0.857 | 0.874 | 0.934 | 0.817 | 0.897 | 0.756 | 0.828 |
| 2 | 137–139‡ | 0.672 | 0.165 | 0.885 | 0.302 | 0.793 | 0.832 | 0.745 |
| 3 | 161–159‡ | 0.739 | 0.305 | 0.819 | 0.508 | 0.838 | 0.889 | 0.902 |
| 4 | 161–164‡ | 0.673 | 0.060 | 0.851 | 0.407 | 0.780 | 0.922 | 0.434 |
| 5 | 169–171‡ | 0.772 | 0.359 | 0.777 | 0.520 | 0.779 | 0.885 | 0.789 |
| 6 | 177–174‡ | 0.846 | 0.893 | 0.942 | 0.463 | 0.851 | 0.949 | 0.903 |
| 7 | 177–175‡ | 0.915 | 0.236 | 0.954 | 0.644 | 0.916 | 0.955 | 0.937 |
| 8 | 185–181‡ | 0.919 | 0.278 | 0.961 | 0.575 | 0.932 | 0.963 | 0.912 |

*The number at the left of "–" is the DOY of the predicted NDVI and the number at the right of "–" is the DOY of the HJ-1 NDVI.


**Figure 8.** Mean and standard deviation (SD) differences for each land cover type from the predicted NDVI and the HJ-1 NDVI on closest DOYs: (a) mean difference, (b) SD difference. Integers (1,2,. . .,8) refer to the DOY listed in **Table 5**. For example, 1 refers to DOY = 129–125; 129 is the DOY of the predicted NDVI, and 125 is the DOY of the HJ-1 NDVI.

A simple average of the various different measurements substantially increased the SD of the field pixel data, and therefore the mean value was used as the main reference point for the pixel NDVI. From these results, it was apparent that the predicted NDVI time series provided a good description of dynamic changes in vegetation. The predicted NDVI was more strongly influenced by the HJ-1 NDVI used in CC. The $R^2$ between the field NDVI mean values and the corresponding pixel NDVI values was 0.8.

### Comparison with STARFM

As visualized in **Figures 7a** and **7b**, vegetation changes in space and time were consistent with the data predicted by STARFM and CC. Image validation was also conducted. $R^2$ values were calculated for all land cover types, but are not shown here. Compared with **Table 5**, meadow and forest have low $R^2$ values which may be due to cloud contamination. The $R^2$ of the remaining land cover types appeared to show the same overall trend, but were a little lower than the corresponding values in **Table 5**. This may have occurred because STARFM introduced more coarse-resolution information that made the high-resolution details fuzzy. When the acquisition time of HJ-1 is far from that of MODIS or when the weighting or window size is not suitable, "patches" of the size of a MODIS pixel will appear, as shown in **Figure 10**. Repeated efforts are needed to reduce the "patches" by adjusting the window size and the weights of neighboring pixels depending on the heterogeneity of the landscape.

### Large-area application

The CC method was used in several plots in China, including the rainy south, the arid and semiarid west, and

Vol. 37, No. 6, December/décembre 2011



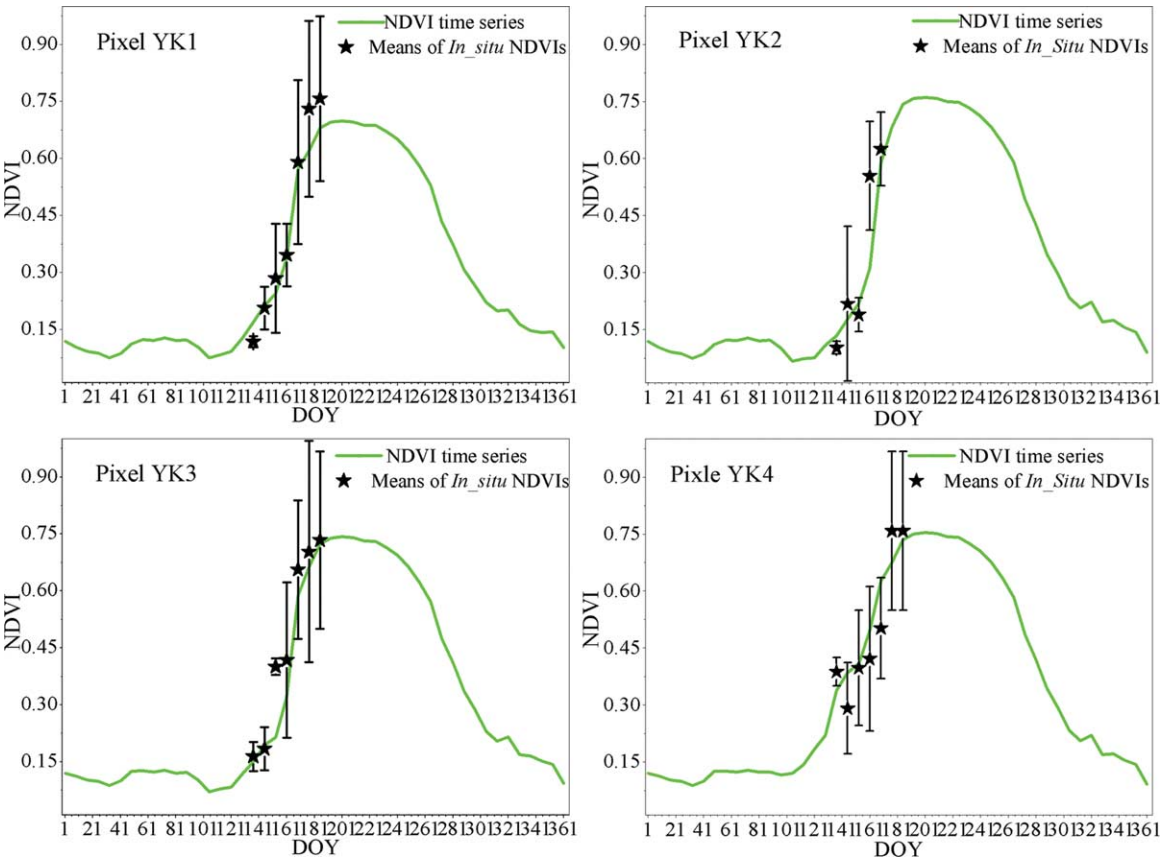


**Figure 9.** Comparison of the 8 day, 30 m predicted NDVI time series with the in situ NDVI.

the temperate middle region. The NDVI was also input to another algorithm to produce time-series vegetation fractions for these plots. In the rainy south plot, only one HJ-1 CCD image was obtained, but the results were reasonable because the vegetation there is evergreen. Comparison with the field vegetation fraction obtained by the traditional visual method yielded good results, as shown in **Figure 11**, which indicates that from another vantage point the CC method can provide a good description of vegetation. The NDVI produced formed part of the input data to the soil erosion model used in the Chinese national soil and water conservation status investigation in 2011. Errors caused by the 30 m

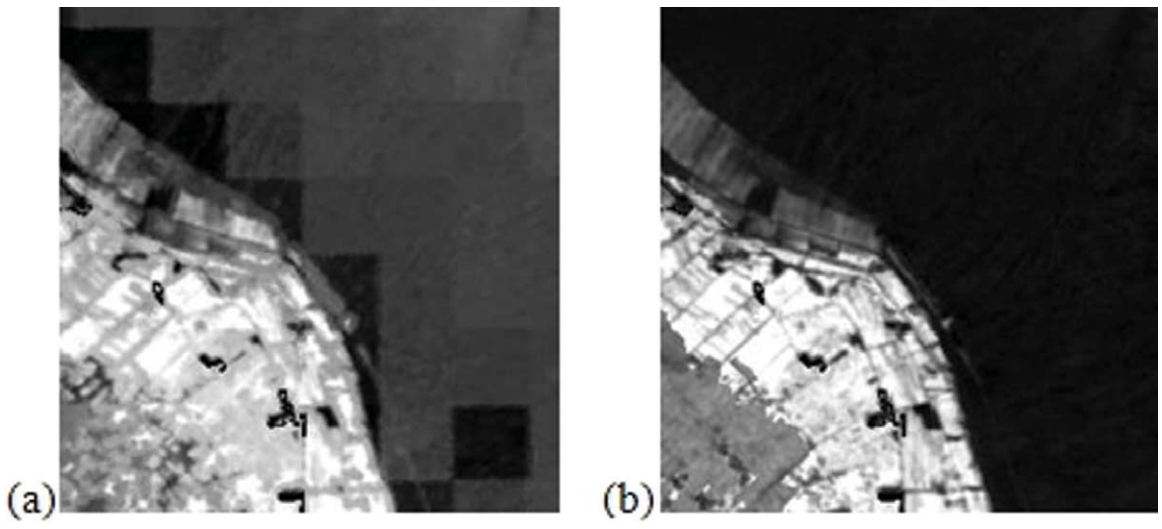


**Figure 10.** "Patches" in the NDVI generated by STARFM: (a) NDVI produced by STARFM, DOY = 265, (b) NDVI produced by CC, DOY = 265.

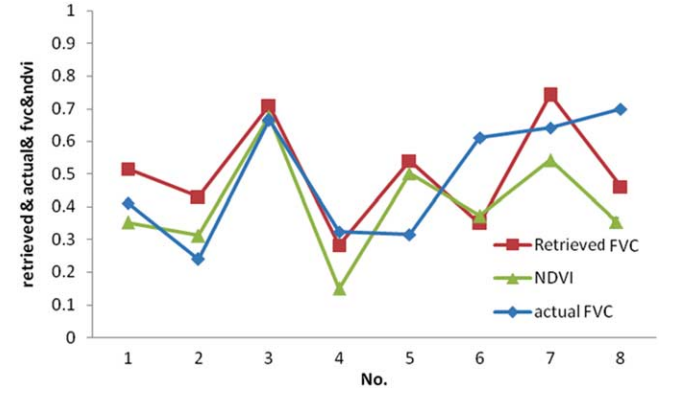


**Figure 11.** Validation by fractional vegetation cover (FVC) field data.

land cover map were considered as misclassifications and also included a registration error if the map was generated from other resources. Other errors arose from a small amount of cloud contamination in the HJ-1 CCD images selected.

## Conclusions

HJ-1 CCD has an enormous advantage and superior capabilities in quantitative remote sensing because of its high spatial resolution. However, noise introduced by cloud contamination and atmospheric variability and other constraints prevents it from being used in applications that need time series data. The MODIS composited reflectance product offered rich temporal information about land surfaces, but its coarse resolution made the information insufficient, especially for heterogeneous landscapes. To use HJ-1 CCD spatial information and MODIS temporal information at the same time, the CC data assimilation method was used to combine the two kinds of data resources to produce a nadir-observed dataset with the CCD spatial resolution and NBAR temporal resolution as if such a satellite is present and observing at nadir. NBAR NDVI was used to provide the multiyear average vegetation growing state, and HJ-1 NDVI was used to adjust this multiyear state to approximate the current state even the future state, because the time series 30 m NDVI can be generated as long as there is HJ-1 data. The MODIS multiyear average NDVI time series and the HJ-1 NDVI of each category were considered as the background field values and the observation values respectively. The data generated by the CC method as well as the validation using in situ data and HJ-1 CCD images indicated good results.

Using the MODIS product, it is hard to obtain high-quality data after quality control for weather conditions, and therefore the STARFM method is limited; otherwise, much noise will be introduced into the predicted data. Another approach is to reconstruct a high quality MODIS dataset according to some reconstruction method, which is a time-consuming task, and moreover, different reconstruction methods have different disadvantages. CC can avoid such problems because its background field values are extracted from several years of data; even if the data are not of high quality, a simple Savitzky–Golay filter (Chen, 2004) can be applied to the average NDVI time series to provide a less noisy background.

Only NBAR and HJ-1 CCD reflectance were used in our study. In practice, other MODIS reflectance products or VI products can be used, and other sensors similar to MODIS and HJ-1 can be substituted or combined according to requirements. Moreover, other kinds of land surface parameters such as reflectance and LAI can be generated using this method.

## Acknowledgements

Many thanks to Mr. Bo Zhong of the Institute of Remote Sensing Applications, Chinese Academy of Sciences, China, for providing the HJ-1 CCD reflectance images and the 30 m land cover map. This research was supported in part by the National Natural Science Foundation of China (No. 41171263, 41171264), the National Soil Erosion Survey Program and the Special Funds for Major State Basic Research Project (2007CB714407).

## References

Anyamba, A., and Tucker, C.J. 2005. Analysis of sahelian vegetation dynamics using NOAA-AVHRR NDVI data from 1981–2003. *Journal of Arid Environments*, Vol. 63, No. 3, pp. 596–614. doi: 10.1016/j.jaridenv.2005.03.007.

Asner, G.P. 2001. Cloud cover in Landsat observations of the Brazilian Amazon. *International Journal of Remote Sensing*, Vol. 22, No. 18, pp. 3855–3862. doi: 10.1080/01431160010006926.

Busetto, L., and Meroni, M. 2008. Combining medium and coarse spatial resolution satellite data to improve the estimation of sub-pixel NDVI time series. *Remote Sensing of Environment*, Vol. 1121, pp. 118–131. doi: 10.1016/j.rse.2007.04.004.

Carlson, T.N., and Ripley, D.A. 1997. On the relation between NDVI, fractional vegetation cover, and leaf area index. *Remote Sensing of Environment*, Vol. 62, No. 3, pp. 241–252. doi: 10.1016/S0034-4257(97)00104-1.

Chen, J., Jönsson, P., Tamura, M., Gu, Z., Matsushita, B., and Eklundh, L. 2004. A simple method for reconstructing a high-quality NDVI time-series data set based on the Savitzky-Golay filter. *Remote Sensing of Environment*, Vol. 91, No. 3–4, pp. 332–344. doi: 10.1016/j.rse.2004.03.014.

Defries, R.S., and Townshend, J.R.G. 1994. NDVI-derived land cover classifications at a global scale. *International Journal of Remote Sensing*, Vol. 15, No. 17, pp. 3567–3586. doi: 10.1080/01431169408954345.

Doktor, D., Bondeau, A., Koslowski, D., and Badeck, F.W. 2009. Influence of heterogeneous landscapes on computed green-up dates based on daily AVHRR NDVI observations. *Remote Sensing of Environment*, Vol. 113, No. 12, pp. 2618–2632. doi: 10.1016/j.rse.2009.07.020.

Gao, F., Masek, J., Schwaller, M., and Hall, F. 2006. On the blending of the Landsat and MODIS surface reflectance: predicting daily Landsat surface reflectance. *IEEE Transactions on Geosciences and Remote Sensing*, Vol. 44, No. 8, pp. 2207–2218. doi: 10.1109/TGRS.2006.872081.

Jarlan, L., Mangiarotti, S., Mougin, E., Mazzega, P., Hiernaux, P., and Dantec, V.L. 2008. Assimilation of SPOT/VEGETATION NDVI data into a Sahelian vegetation dynamics model. *Remote Sensing of Environment*, Vol. 112, No. 4, pp. 1381–1394. doi: 10.1016/j.rse.2007.02.041.

Jiang, Z., Huete, A.R., Chen, J., Chen, Y., Li, J., Yan, G., and Zhang, X. 2006. Analysis of NDVI and scaled difference vegetation index retrievals of vegetation fraction. *Remote Sensing of Environment*, Vol. 3, No. 101, pp. 366–378. doi: 10.1016/j.rse.2006.01.003.

Knorn, J., Rabe, A., Radeloff, V.V., Kuemmerle, T., Kozak, J., and Hostert, P. 2009. Land cover mapping of large areas using chain classification of neighboring Landsat satellite images. *Remote Sensing of Environment*, Vol. 113, No. 5, pp. 957–964. doi: 10.1016/j.rse.2009.01.010.

Lee, T.Y., and Kaufman, Y.J. 1986. Non-Lambertian effects on remote sensing of surface reflectance and vegetation index. *IEEE Transactions on Geoscience and Remote Sensing*, Vol. GE-24, No. 5, pp. 699–708. doi: 10.1109/TGRS.1986.289617.

Li, C.R., Jia, Y.Y., Hu, J., and Li, Z.Y. 2008. An analysis of the prospects of the HJ-1 optical satellite in a remote sensing application. *Remote Sensing for Land and Resources*, Vol. 77, No. 3, pp. 1–4.

Li, X., Li, X.W., Li, Z., Ma, M., Wang, J., Xiao, Q., Liu, Q., Che, T., Chen, E., et al. 2009. Watershed allied telemetry experimental research. *Journal of Geophysical Research*, Vol. 114, pp. 1–19, D22103, doi: 10.1029/2008JD011590.

Li, Y., Wang, X., and Liu, B. 2009. Researches on HJ-1 satellite image quality and land-use classification precision. *Remote Sensing for Land and Resources*, Vol. 81, No. 3, pp. 74–77.

Liang, S. 2009. *Quantitative Remote Sensing of Land Surface*. Science Press, Beijing.

Liang, S., Fang, H., and Chen, M. 2001. Atmospheric correction of Landsat ETM + land surface imagery: Part I: methods. *IEEE Transactions on Geosciences and Remote Sensing*, Vol. 39, No. 11, pp. 2490–2498. doi: 10.1109/36.964986.

Lopes, D.M., Aranha, J.T., Walford, N., O'Brien, J., and Lucas, N. 2009. Accuracy of remote sensing data versus other sources of information for estimating net primary production in *Eucalyptus globulus Labill* and *Pinus pinaster Ait.* ecosystems in Portugal. *Canadian Journal of Remote Sensing*, Vol. 35, No. 1, pp. 37–53. doi: 10.5589/m08-078.

Lunetta, R.S., Knight, J.F., Ediriwickrema, J., Lyon, O.G., and Worthy, L.D. 2006. Land-cover change detection using multi-temporal MODIS NDVI data. *Remote Sensing of Environment*, Vol. 115, No. 30, pp. 142–154. doi: 10.1016/j.rse.2006.06.018.

Martínez, B., and Gilbert, M.A. 2009. Vegetation dynamics from NDVI time series analysis using the wavelet transform. *Remote Sensing of Environment*, Vol. 113, No. 9, pp. 1823–1842. doi: 10.1016/j.rse.2009.04.016.

Maselli, F., Gilbert, M.A., and Conese, C. 1998. Integration of high- and low-resolution NDVI data for monitoring vegetation in Mediterranean environments. *Remote Sensing of Environment*, Vol. 63, No. 3, pp. 208–218. doi: 10.1016/S0034-4257(97)00131-4.

Oetter, D.R., Cohen, W.B., Berterretche, M., Maiersperger, T.K., and Kennedy, R.R. 2001. Land cover mapping in an agricultural setting using multiseasonal Thematic Mapper data. *Remote Sensing of Environment*, Vol. 76, No. 2, pp. 139–155. doi: 10.1016/S0034-4257(00)00202-9.

Piao, S., Mohammat, A., Fang, J., Cai, Q., and Feng, J. 2006. NDVI-based increase in growth of temperate grasslands and its responses to climate changes in China. *Global Environmental Change*, Vol. 16, No. 4, pp. 340–348. doi: 10.1016/j.gloenvcha.2006.02.002.

Potter, C.S., and Brooks, V. 1998. Global analysis of empirical relations between annual climate and seasonality of NDVI. *International Journal of Remote Sensing*, Vol. 19, No. 15, pp. 2921–2948. doi: 10.1080/014311698214352.

Ri, P., Ma, Z., Qi, Q., and Liu, G. 2010. Cloud and shadow removal from Landsat TM data. *Journal of Remote Sensing*, Vol. 3, pp. 534–545.

Roy, D.P., Ju, J., Lewis, P., Schaaf, C., Gao, F., Hansen, M., and Lindquist, E. 2008. Multi-temporal MODIS and Landsat data fusion for relative radiometric normalization, gap filling, and prediction of Landsat data. *Remote Sensing of Environment*, Vol. 112, pp. 3112–3130. doi: 10.1016/j.rse.2008.03.009.

Schaaf, C.B., Gao, F., Strahler, A.H., Lucht, W., Li, X., Tsang, T., Strugnell, N.C., Zhang, X., Jin, Y., Muller, J.P., et al. 2002. First operational BRDF, albedo nadir reflectance products from MODIS. *Remote Sensing of Environment*, Vol. 83, No. 1–2, pp. 135–148. doi: 10.1016/S0034-4257(02)00091-3.

Senay, G.B., and Elliott, R.L. 2000. Combining AVHRR-NDVI and landuse data to describe temporal and spatial dynamics of vegetation. *Forest Ecology and Management*, Vol. 128, pp. 83–91. doi: 10.1016/S0378-1127(99)00275-3.

Shabanov, N.V., Wang, Y., Buermann, W., Dong, J., Hoffman, S., Smith, G.R., Tian, Y., Knyazikhin, Y., and Myneni, R.B. 2003. Effect of foliage spatial heterogeneity in the MODIS LAI and FPAR algorithm over broadleaf forests. *Remote Sensing of Environment*, Vol. 85, No. 4, pp. 410–423. doi: 10.1016/S0034-4257(03)00017-8.

Stefanov, W.L., and Netzband, M. 2005. Assessment of ASTER land cover and MODIS NDVI data at multiple scales for ecological characterization of an arid urban center. *Remote Sensing of Environment*, Vol. 99, No. 1–2, pp. 31–43. doi: 10.1016/j.rse.2005.04.024.

Wan, H., Wang, J., Qu, Y., Jiao, Z., and Zhang, H. 2008. Preliminary research on scale effect and scaling up of the vegetation spectrum. *Journal of Remote Sensing*, Vol. 4, No. 12, pp. 538–545.

Wang, J., Liu, Y., Fang, Z., Yang, S., Nie, J., Wu, W., Liu, S., Wang, L., Wang, Q., Wei, B., et al. 2010. Operation and application of A, B satellites for environment and disaster monitoring and forecasting. *Chinese Journal of Space Science*, Vol. 30, No. 5, pp. 486–492.

Wang, Q., Wu, C., and Li, Q. 2010. Environment Satellite 1 and its application in environmental monitoring. *Journal of Remote Sensing*, Vol. 14, No. 1, pp. 104–121.

Weiss, J.L., Gutzler, D.S., Coonrod, J.E.A., and Dahm, C.N. 2004. Long-term vegetation monitoring with NDVI in a diverse semi-arid setting, central New Mexico, USA. *Journal of Arid Environments*, Vol. 58, No. 2, pp. 249–272. doi: 10.1016/j.jaridenv.2003.07.001.

Zhang, M., Dong, Q., Tang, J., and Song, Q. 2010. Evaluation of the retrieval of total suspended matter concentration in Taihu Lake, China from CBERS-02B CCD. *Chinese Journal of Oceanology and Limnology*, Vol. 28, No. 6, pp. 1316–1322. doi: 10.1007/s00343-010-9948-7.

Zhao, Y. 2003. *Principles and Methods of Remote Sensing Applications*. Science Press, Beijing.